APRIL 13 2018

A higher-order “figure-8” sensor and an isotropic sensor—For azimuth-elevation bivariate direction finding

Muhammad Muaz; Yue Ivan Wu; Kainam Thomas Wong; Da Su

J. Acoust. Soc. Am. 143, 2041–2054 (2018)
https://doi.org/10.1121/1.5027844

A higher-order "figure-8" sensor and an isotropic sensor—For azimuth-elevation bivariate direction finding

Muhammad Muaz
Department of Electronic & Information Engineering, The Hong Kong Polytechnic University, Hong Kong Special Administrative Region

Yue Ivan Wu
College of Computer Science, Sichuan University, Chengdu, Sichuan, China

Kainam Thomas Wong[a] and Da Su
Department of Electronic & Information Engineering, The Hong Kong Polytechnic University, Hong Kong Special Administrative Region

(Received 9 August 2017; revised 1 March 2018; accepted 6 March 2018; published online 13 April 2018)

A "p-u probe" (also known as a "p-v probe") comprises one pressure-sensor (which is isotropic) and one uni-axial particle-velocity sensor (which has a "figure-8" bi-directional spatial directivity). This p-u probe may be generalized, by allowing the figure-8 bi-directional sensor to have a higher order of directivity. This higher-order p-u probe has not previously been investigated anywhere in the open literature (to the best knowledge of the present authors). For such a sensing system, this paper is first (1) to develop closed-form eigen-based signal-processing algorithms for azimuth-elevation direction finding; (2) to analytically derive the associated Cramér-Rao lower bounds (CRB), which are expressed explicitly in terms of the two constituent sensors' spatial geometry and in terms of the figure-8 sensor's directivity order; (3) to verify (via Monte Carlo simulations) the proposed direction-of-arrival estimators' efficacy and closeness to the respective CRB. Here, the higher-order p-u probe's two constituent sensors may be spatially displaced.

https://doi.org/10.1121/1.5027844

[JFL] Pages: 2041–2054

I. INTRODUCTION

The "p-u probe" is an acoustical sensing system popular for air acoustics and underwater acoustics. The p-u probe consists of (a) an isotropic *p*ressure-sensor, which is isotropic in its gain-response, (b) a uni-axial particle- *v*elocity sensor, whose gain-response is bi-directional, like a "figure-8," i.e., $\cos(\gamma)$ in mathematical form, where γ represents the angle from the directional sensor's axis. Such a uni-axial particle-velocity sensor measures one Cartesian component of the acoustical wavefield's particle velocity vector.

For a listing of the key literature on p-u probes, please refer to Ref. 1.

This figure-8 directivity could be sharpened through the use of a higher-order sensor, to give a $\cos^k(\gamma)$ directivity (see Sec. 8.5. of Ref. 2 and Sec. 5 of Chap. 2 in Ref. 3):

(i) If a kth-order figure-8 sensor is oriented along the x axis, its gain response equals $[\sin(\theta)\cos(\phi)]^k$. Here, $\theta \in [0, \pi]$ represents the polar angle (also known as the zenith angle), and $\phi \in [0, 2\pi)$ denotes the azimuth angle measured from the positive x axis.
(ii) If oriented along the y-axis, the gain response becomes $[\sin(\theta)\sin(\phi)]^k$.
(iii) If oriented along the z-axis, the gain response becomes $\cos^k(\theta)$.

Please see Ref. 4 for a brief discussion of higher-order figure-8 sensors. (The particle-velocity sensor has an order of $k = 1$, whereas the isotropic pressure-sensor has an order of $k = 0$.) This paper generalizes the customary p-u probe, by allowing the figure-8 sensor to have any arbitrarily higher (integer) order k of directivity.

Second-order figure-8 bi-directional acoustic sensors have been implemented in hardware in Refs. 5–16 Third-order figure-8 bi-directional acoustic sensors have been implemented in hardware in Refs. 10, 14, and 17. Fifth-order figure-8 bi-directional acoustic sensors have been implemented in hardware in Ref. 18. Other higher-order figure-8 bi-directional acoustic sensors have been implemented in hardware in Refs. 10–14. These hardware implementations of *second*-order or *higher*-order p-u probes, dating from 1942 to 2008, show that second-order/higher-order p-u probes are established yet current sensing systems with continuing practical relevance.

Specifically, suppose that the isotropic sensor (i.e., a pressure-sensor) is placed at the Cartesian origin, and suppose that the figure-8 sensor lies on one of the three Cartesian axes and is also oriented in parallel to one of the Cartesian axes. Then, there would be nine distinct combinations of the figure-8 sensor's location and axial orientation. Please see Fig. 1. Figure 1(a), for example, corresponds to a pressure sensor at the Cartesian origin, with a figure-8 directional sensor at the Cartesian position of $(\Delta_x, 0, 0)$ but orienting along the x axis. Figure 1(b), in contrast, has the figure-8 directional sensor at

---

[a] Electronic mail: ktwong@ieee.org

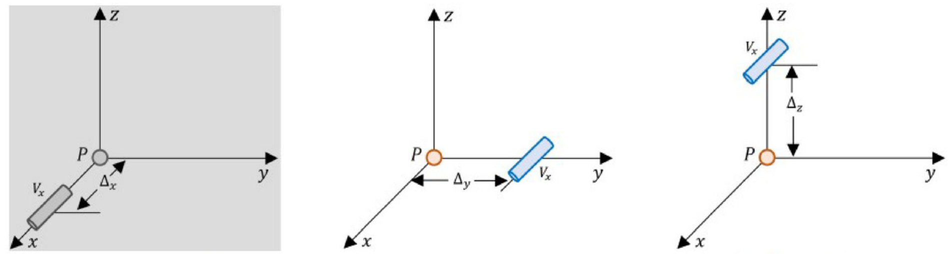

(a) V_x at $(\Delta_x, 0, 0)$ (b) V_x at $(0, \Delta_y, 0)$ (c) V_x at $(0, 0, \Delta_z)$

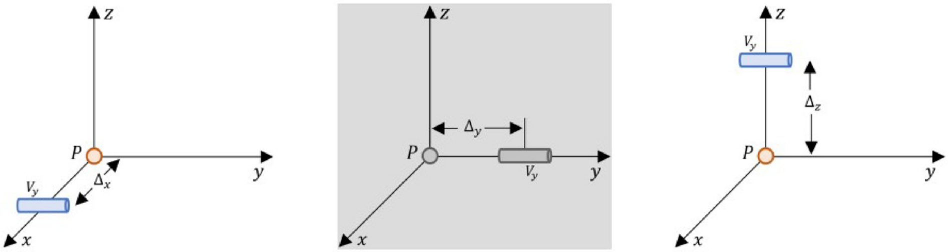

(d) V_y at $(\Delta_x, 0, 0)$ (e) V_y at $(0, \Delta_y, 0)$ (f) V_y at $(0, 0, \Delta_z)$

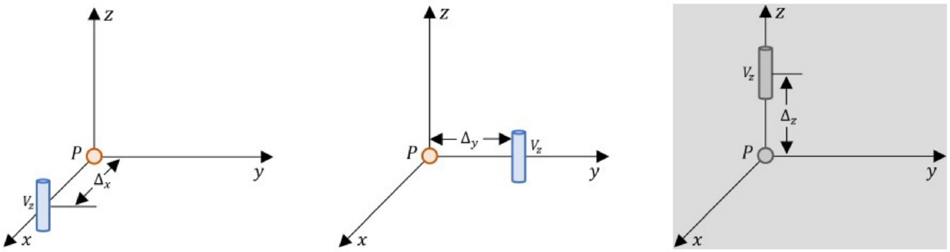

(g) V_z at $(\Delta_x, 0, 0)$ (h) V_z at $(0, \Delta_y, 0)$ (i) V_z at $(0, 0, \Delta_z)$

FIG. 1. (Color online) The higher-order p-u probe's nine configurations under investigation. The shaded configurations cannot facilitate bivariate azimuth-elevation direction-of-arrival estimation. Please see Sec. III. (a) V_x at $(\Delta_x, 0, 0)$, (b) V_x at $(0, \Delta_y, 0)$, (c) V_x at $(0, 0, \Delta_z)$, (d) V_y at $(\Delta_x, 0, 0)$, (e) V_y at $(0, \Delta_y, 0)$, (f) V_y at $(0, 0, \Delta_z)$, (g) V_z at $(\Delta_x, 0, 0)$, (h) V_z at $(0, \Delta_y, 0)$, (i) V_z at $(0, 0, \Delta_z)$.

the Cartesian position of $(0, \Delta_y, 0)$ but still orienting along the x axis.

For each of these nine configurations at any specific sensor-order k: Section II will define its array manifold. Section III will derive a new closed-form estimator of the incident source's azimuth-elevation bivariate direction-of-arrival (or, for three of the nine array configurations, will explain why such an estimator is mathematically impossible). Section IV will analytically derive the corresponding Cramér-Rao lower bound, in a simple mathematical form that is explicitly in terms of the array geometry and explicitly in terms of sensor order k. Section V will then present Monte Carlo simulations of the proposed estimator, showing its closeness to the derived Cramér-Rao lower bound. Last, Sec. VI will conclude the entire paper.

TABLE I. The array manifold for various configurations of kth-order p-u probe. [Please see Eq. (1).]

configuration (a): $\mathbf{a}^{(x)}_{P,V_x}(\theta,\phi) = \begin{bmatrix} 1 \\ u^k \quad e^{j2\pi(\Delta_x/\lambda)u} \end{bmatrix}$	configuration (b): $\mathbf{a}^{(y)}_{P,V_x}(\theta,\phi) = \begin{bmatrix} 1 \\ u^k \quad e^{j2\pi(\Delta_y/\lambda)v} \end{bmatrix}$	configuration (c): $\mathbf{a}^{(z)}_{P,V_x}(\theta,\phi) = \begin{bmatrix} 1 \\ u^k \quad e^{j2\pi(\Delta_z/\lambda)w} \end{bmatrix}$
configuration (d): $\mathbf{a}^{(x)}_{P,V_y}(\theta,\phi) = \begin{bmatrix} 1 \\ v^k \quad e^{j2\pi(\Delta_x/\lambda)u} \end{bmatrix}$	configuration (e): $\mathbf{a}^{(y)}_{P,V_y}(\theta,\phi) = \begin{bmatrix} 1 \\ v^k \quad e^{j2\pi(\Delta_y/\lambda)v} \end{bmatrix}$	configuration (f): $\mathbf{a}^{(z)}_{P,V_y}(\theta,\phi) = \begin{bmatrix} 1 \\ v^k \quad e^{j2\pi(\Delta_z/\lambda)w} \end{bmatrix}$
configuration (g): $\mathbf{a}^{(x)}_{P,V_z}(\theta,\phi) = \begin{bmatrix} 1 \\ w^k \quad e^{j2\pi(\Delta_x/\lambda)u} \end{bmatrix}$	configuration (h): $\mathbf{a}^{(y)}_{P,V_z}(\theta,\phi) = \begin{bmatrix} 1 \\ w^k \quad e^{j2\pi(\Delta_y/\lambda)v} \end{bmatrix}$	configuration (i): $\mathbf{a}^{(z)}_{P,V_z}(\theta,\phi) = \begin{bmatrix} 1 \\ w^k \quad e^{j2\pi(\Delta_z/\lambda)w} \end{bmatrix}$

TABLE II. Closed-form estimates $(\hat{\theta},\ \hat{\phi})$ of the azimuth-elevation bivariate direction-of-arrival, for the various configurations.

#	"figure-8" sensor's location	"figure-8" sensor's orientation	$(\hat{\theta}, \hat{\phi})$
(a)	$(\Delta_x, 0, 0)$	x-axis	$\hat{\theta}, \hat{\phi}$ unobtainable.
(b)	$(0, \Delta_y, 0)$	x-axis	$\hat{\theta} = \begin{cases} \sin^{-1}\left(\mathrm{sgn}(u)\sec(\hat{\phi})\left\lvert\frac{\left[\hat{\mathbf{a}}^{(y)}_{P,V_x}\right]_2}{\left[\hat{\mathbf{a}}^{(y)}_{P,V_x}\right]_1}\right\rvert^{1/k}\right), & \text{if } \theta \in \left[0, \frac{\pi}{2}\right); \\ \pi - \sin^{-1}\left(\mathrm{sgn}(u)\sec(\hat{\phi})\left\lvert\frac{\left[\hat{\mathbf{a}}^{(y)}_{P,V_x}\right]_2}{\left[\hat{\mathbf{a}}^{(y)}_{P,V_x}\right]_1}\right\rvert^{1/k}\right), & \text{if } \theta \in \left[\frac{\pi}{2}, \pi\right). \end{cases}$ $\hat{\phi} = \begin{cases} \frac{\pi}{2}\left[\lvert\mathrm{sgn}(u)\rvert - \mathrm{sgn}(u)\right] \\ \quad +\tan^{-1}\left(\frac{1}{2\pi}\frac{\lambda}{\Delta_y}\angle\left(\mathrm{sgn}(u)\,\frac{\left[\hat{\mathbf{a}}^{(y)}_{P,V_x}\right]_2}{\left[\hat{\mathbf{a}}^{(y)}_{P,V_x}\right]_1}\right)\left\lvert\frac{\left[\hat{\mathbf{a}}^{(y)}_{P,V_x}\right]_1}{\left[\hat{\mathbf{a}}^{(y)}_{P,V_x}\right]_2}\right\rvert^{1/k}\right). \end{cases}$
(c)	$(0, 0, \Delta_z)$	x-axis	$\hat{\theta} = \cos^{-1}\left(\frac{1}{2\pi}\frac{\lambda}{\Delta_z}\angle\left(\mathrm{sgn}(u)\,\frac{\left[\hat{\mathbf{a}}^{(z)}_{P,V_x}\right]_2}{\left[\hat{\mathbf{a}}^{(z)}_{P,V_x}\right]_1}\right)\right).$ $\hat{\phi} = \begin{cases} \cos^{-1}\left(\csc(\hat{\theta})\left\lvert\frac{\left[\hat{\mathbf{a}}^{(z)}_{P,V_x}\right]_2}{\left[\hat{\mathbf{a}}^{(z)}_{P,V_x}\right]_1}\right\rvert^{1/k}\mathrm{sgn}(u)\right), & \text{if } \phi \in [0, \pi); \\ 2\pi - \cos^{-1}\left(\csc(\hat{\theta})\left\lvert\frac{\left[\hat{\mathbf{a}}^{(z)}_{P,V_x}\right]_2}{\left[\hat{\mathbf{a}}^{(z)}_{P,V_x}\right]_1}\right\rvert^{1/k}\mathrm{sgn}(u)\right), & \text{if } \phi \in [\pi, 2\pi). \end{cases}$
(d)	$(\Delta_x, 0, 0)$	y-axis	$\hat{\theta} = \begin{cases} \sin^{-1}\left(\mathrm{sgn}(v)\csc(\hat{\phi})\left\lvert\frac{\left[\hat{\mathbf{a}}^{(x)}_{P,V_y}\right]_2}{\left[\hat{\mathbf{a}}^{(x)}_{P,V_y}\right]_1}\right\rvert^{1/k}\right), & \text{if } \theta \in \left[0, \frac{\pi}{2}\right); \\ \pi - \sin^{-1}\left(\mathrm{sgn}(v)\csc(\hat{\phi})\left\lvert\frac{\left[\hat{\mathbf{a}}^{(x)}_{P,V_y}\right]_2}{\left[\hat{\mathbf{a}}^{(x)}_{P,V_y}\right]_1}\right\rvert^{1/k}\right), & \text{if } \theta \in \left[\frac{\pi}{2}, \pi\right). \end{cases}$ $\hat{\phi} = \begin{cases} \frac{\pi}{2}\left[\lvert\mathrm{sgn}(u)\rvert - \mathrm{sgn}(u)\right] \\ \quad +\tan^{-1}\left[2\pi\frac{\Delta_x}{\lambda}\left\{\angle\left(\mathrm{sgn}(v)\,\frac{\left[\hat{\mathbf{a}}^{(x)}_{P,V_y}\right]_2}{\left[\hat{\mathbf{a}}^{(x)}_{P,V_y}\right]_1}\right)\right\}^{-1}\left\lvert\frac{\left[\hat{\mathbf{a}}^{(x)}_{P,V_y}\right]_2}{\left[\hat{\mathbf{a}}^{(x)}_{P,V_y}\right]_1}\right\rvert^{1/k}\right]. \end{cases}$
(e)	$(0, \Delta_y, 0)$	y-axis	$\hat{\theta}, \hat{\phi}$ unobtainable.
(f)	$(0, 0, \Delta_z)$	y-axis	$\hat{\theta} = \cos^{-1}\left(\frac{1}{2\pi}\frac{\lambda}{\Delta_z}\angle\left(\mathrm{sgn}(v)\,\frac{\left[\hat{\mathbf{a}}^{(z)}_{P,V_y}\right]_2}{\left[\hat{\mathbf{a}}^{(z)}_{P,V_y}\right]_1}\right)\right).$ $\hat{\phi} = \begin{cases} \pi(\lvert\mathrm{sgn}(v)\rvert - \mathrm{sgn}(v)) & \\ \quad +\sin^{-1}\left(\csc(\hat{\theta})\left\lvert\frac{\left[\hat{\mathbf{a}}^{(z)}_{P,V_y}\right]_2}{\left[\hat{\mathbf{a}}^{(z)}_{P,V_y}\right]_1}\right\rvert^{1/k}\mathrm{sgn}(v)\right), & \text{if } \phi \in \left[-\frac{\pi}{2}, \frac{\pi}{2}\right); \\ \pi - \sin^{-1}\left(\csc(\hat{\theta})\left\lvert\frac{\left[\hat{\mathbf{a}}^{(z)}_{P,V_y}\right]_2}{\left[\hat{\mathbf{a}}^{(z)}_{P,V_y}\right]_1}\right\rvert^{1/k}\mathrm{sgn}(v)\right), & \text{if } \phi \in \left[\frac{\pi}{2}, \frac{3\pi}{2}\right). \end{cases}$

TABLE II. (*Continued*)

#	"figure-8" sensor's location	"figure-8" sensor's orientation	$(\hat{\theta}, \hat{\phi})$
(g)	$(\Delta_x, 0, 0)$	z-axis	$\hat{\theta} = \cos^{-1}\left(\mathrm{sgn}(w)\left\lvert\frac{\left[\hat{\mathbf{a}}^{(x)}_{P,V_z}\right]_2}{\left[\hat{\mathbf{a}}^{(x)}_{P,V_z}\right]_1}\right\rvert^{1/k}\right).$ $\hat{\phi} = \begin{cases} \cos^{-1}\left(\frac{1}{2\pi}\frac{\lambda}{\Delta_x}\csc(\hat{\theta})\angle\left(\mathrm{sgn}(w)\,\frac{\left[\hat{\mathbf{a}}^{(x)}_{P,V_z}\right]_2}{\left[\hat{\mathbf{a}}^{(x)}_{P,V_z}\right]_1}\right)\right), & \text{if } \phi \in [0, \pi); \\ 2\pi - \cos^{-1}\left(\frac{1}{2\pi}\frac{\lambda}{\Delta_x}\csc(\hat{\theta})\angle\left(\mathrm{sgn}(w)\,\frac{\left[\hat{\mathbf{a}}^{(x)}_{P,V_z}\right]_2}{\left[\hat{\mathbf{a}}^{(x)}_{P,V_z}\right]_1}\right)\right), & \text{if } \phi \in [\pi, 2\pi). \end{cases}$
(h)	$(0, \Delta_y, 0)$	z-axis	$\hat{\phi} = \begin{cases} \sin^{-1}\left(\frac{1}{2\pi}\frac{\lambda}{\Delta_y}\csc(\hat{\theta})\angle\left(\mathrm{sgn}(w)\,\frac{\left[\hat{\mathbf{a}}^{(y)}_{P,V_z}\right]_2}{\left[\hat{\mathbf{a}}^{(y)}_{P,V_z}\right]_1}\right)\right), & \text{if } \phi \in \left[-\frac{\pi}{2}, \frac{\pi}{2}\right); \\ 2\pi - \sin^{-1}\left(\frac{1}{2\pi}\frac{\lambda}{\Delta_y}\csc(\hat{\theta})\angle\left(\mathrm{sgn}(w)\,\frac{\left[\hat{\mathbf{a}}^{(y)}_{P,V_z}\right]_2}{\left[\hat{\mathbf{a}}^{(y)}_{P,V_z}\right]_1}\right)\right), & \text{if } \phi \in \left[\frac{\pi}{2}, \frac{3\pi}{2}\right). \end{cases}$ $\hat{\theta} = \cos^{-1}\left(\left\lvert\frac{\left[\hat{\mathbf{a}}^{(y)}_{P,V_z}\right]_2}{\left[\hat{\mathbf{a}}^{(y)}_{P,V_z}\right]_1}\right\rvert^{1/k}\mathrm{sgn}(w)\right).$
(i)	$(0, 0, \Delta_z)$	z-axis	$\hat{\theta} = \begin{cases} \cos^{-1}\left(\left\lvert\frac{\left[\hat{\mathbf{a}}^{(z)}_{P,V_z}\right]_2}{\left[\hat{\mathbf{a}}^{(z)}_{P,V_z}\right]_1}\right\rvert^{1/k}\right), \\ \text{when } \left\lvert\left\lvert\frac{\left[\hat{\mathbf{a}}^{(z)}_{P,V_z}\right]_2}{\left[\hat{\mathbf{a}}^{(z)}_{P,V_z}\right]_1}\right\rvert^{1/k} - \frac{1}{2\pi}\frac{\lambda}{\Delta_z}\angle\left(\frac{\left[\hat{\mathbf{a}}^{(z)}_{P,V_z}\right]_2}{\left[\hat{\mathbf{a}}^{(z)}_{P,V_z}\right]_1}\right)\right\rvert < \left\lvert-\left\lvert\frac{\left[\hat{\mathbf{a}}^{(z)}_{P,V_z}\right]_2}{\left[\hat{\mathbf{a}}^{(z)}_{P,V_z}\right]_1}\right\rvert^{1/k} - \frac{1}{2\pi}\frac{\lambda}{\Delta_z}\angle\left(-\frac{\left[\hat{\mathbf{a}}^{(z)}_{P,V_z}\right]_2}{\left[\hat{\mathbf{a}}^{(z)}_{P,V_z}\right]_1}\right)\right\rvert; \\ \cos^{-1}\left(-\left\lvert\frac{\left[\hat{\mathbf{a}}^{(z)}_{P,V_z}\right]_2}{\left[\hat{\mathbf{a}}^{(z)}_{P,V_z}\right]_1}\right\rvert^{1/k}\right), \\ \text{when } \left\lvert\left\lvert\frac{\left[\hat{\mathbf{a}}^{(z)}_{P,V_z}\right]_2}{\left[\hat{\mathbf{a}}^{(z)}_{P,V_z}\right]_1}\right\rvert^{1/k} - \frac{1}{2\pi}\frac{\lambda}{\Delta_z}\angle\left(\frac{\left[\hat{\mathbf{a}}^{(z)}_{P,V_z}\right]_2}{\left[\hat{\mathbf{a}}^{(z)}_{P,V_z}\right]_1}\right)\right\rvert > \left\lvert-\left\lvert\frac{\left[\hat{\mathbf{a}}^{(z)}_{P,V_z}\right]_2}{\left[\hat{\mathbf{a}}^{(z)}_{P,V_z}\right]_1}\right\rvert^{1/k} - \frac{1}{2\pi}\frac{\lambda}{\Delta_z}\angle\left(-\frac{\left[\hat{\mathbf{a}}^{(z)}_{P,V_z}\right]_2}{\left[\hat{\mathbf{a}}^{(z)}_{P,V_z}\right]_1}\right)\right\rvert. \end{cases}$ $\hat{\phi}$ unobtainable

This paper thus presents the higher-order p-u probe as an alternative to existing sensing systems, like the "v-v probe,"[19] or the tri-axial velocity sensor,[20,21] or the four-component acoustic vector-sensor (AVS) consisting of a tri-axial velocity sensor and a pressure-sensor.[22–24,33,34] The use of a pressure sensor (instead of additional figure-8 sensors) may simplify the hardware and any calibration.

II. THE ARRAY MANIFOLDS OF THE GENERALIZED P-U PROBE'S NINE CONFIGURATIONS UNDER INVESTIGATION

Any location/orientation configuration of Fig. 1 may have its 2×1 array manifold represented as

$$\mathbf{a}^{(\varepsilon)}_{P,V_\zeta}(\theta, \phi) = \begin{bmatrix} 1 \\ \eta_1^k\, e^{j2\pi(\Delta_\varepsilon/\lambda)\eta_2} \end{bmatrix}. \tag{1}$$

The first entry refers to the isotropic sensor at the Cartesian origin, whereas the second entry corresponds to the figure-8 directional sensor placed away from the Cartesian origin. Here, the superscript $\varepsilon \in \{x, y, z\}$ identifies the Cartesian axis on which the figure-8 sensor lies, the subscript $\zeta \in \{x, y, z\}$ indicates the orientation of figure-8 sensor, and

$$\eta_1 := \begin{cases} \sin(\theta)\cos(\phi), & \text{if } \zeta = x; \\ \sin(\theta)\sin(\phi), & \text{if } \zeta = y; \\ \cos(\theta), & \text{if } \zeta = z; \end{cases}$$

$$\eta_2 := \begin{cases} \sin(\theta)\cos(\phi), & \text{if } \varepsilon = x; \\ \sin(\theta)\sin(\phi), & \text{if } \varepsilon = y; \\ \cos(\theta), & \text{if } \varepsilon = z. \end{cases}$$

The first entry's magnitude equals unity, on account of the pressure-sensor's isotropicity. It has no complex phase, because of its location at the Cartesian origin, hence no spatial phase factor. The second entry's magnitude of η_1^k corresponds to the kth-order figure-8 gain pattern oriented along the ζ Cartesian coordinate. The second entry's complex phase $e^{j2\pi(\Delta_\varepsilon/\lambda)\eta_2}$ represents a spatial phase factor for the figure-8 sensor's location of $\Delta_\varepsilon \approx 0$ on the ε Cartesian coordinate. The sign of the real-valued scalar η_1 specifies the hemisphere from which the source impinges. For example, at $\zeta = z$, $\text{sgn}(\eta_1) = \text{sgn}(\cos(\theta)) > 0$ would mean that the source impinges from the upper hemisphere, whereas $\text{sgn}(\eta_1) = \text{sgn}(\cos(\theta)) < 0$ means the lower hemisphere. Here, $\text{sgn}(\cdot)$ refers to the sign of the real-valued scalar inside the parentheses.

Figure 1's nine location/orientation configurations' array manifolds are presented in Table I. These nine array manifolds are functionally inter-related:

$$(\text{b}) \leftrightarrow (\text{d}) : \mathbf{a}_{P,V_y}^{(x)}(\theta,\phi) = \mathbf{a}_{P,V_x}^{(y)}\left(\theta, \frac{\pi}{2} - \phi\right), \tag{2}$$

$$(\text{c}) \leftrightarrow (\text{f}) : \mathbf{a}_{P,V_x}^{(z)}(\theta,\phi) = \mathbf{a}_{P,V_y}^{(z)}\left(\theta, \frac{\pi}{2} - \phi\right), \tag{3}$$

$$(\text{g}) \leftrightarrow (\text{h}) : \mathbf{a}_{P,V_z}^{(y)}(\theta,\phi) = \mathbf{a}_{P,V_z}^{(x)}\left(\theta, \frac{\pi}{2} - \phi\right), \tag{4}$$

$$(\text{e}) \leftrightarrow (\text{a}) : \mathbf{a}_{P,V_y}^{(y)}(\theta,\phi) = \mathbf{a}_{P,V_x}^{(x)}\left(\theta, \frac{\pi}{2} - \phi\right), \tag{5}$$

$$(\text{i}) \leftrightarrow (\text{a}) \leftrightarrow (\text{e}) : \mathbf{a}_{P,V_z}^{(z)}(\theta,\phi) = \mathbf{a}_{P,V_x}^{(x)}\left(\frac{\pi}{2} - \theta, 0\right) \tag{6}$$

$$= \mathbf{a}_{P,V_y}^{(y)}\left(\frac{\pi}{2} - \theta, \frac{\pi}{2}\right). \tag{7}$$

Last, if the locations of two component-sensors are interchanged, the resulting array manifold is obtainable from the old one by a complex conjugation, then a multiplication by $e^{j2\pi(\Delta_\varepsilon/\lambda)\eta_2}$.

III. EIGEN-BASED CLOSED-FORM ESTIMATION OF THE AZIMUTH-ELEVATION DIRECTION-OF-ARRIVAL

Eigen-based direction-of-arrival estimation involves an intermediate algorithmic step, wherein the incident signal's steering vector is estimated to within an unknown complex-valued scalar c. This unknown c arises from the eigen-decomposition of the data-correlation matrix. (Suppose $\mathbf{e}$ is a eigenvector of the data-correlation matrix, then $c\mathbf{e}$ must also be a valid eigenvector $\forall c \neq 0$.) That is, available to subsequent algorithmic steps is a steering-vector estimate, $\hat{\mathbf{a}}_{P,V_\zeta}^{(\varepsilon)} \approx c\, \mathbf{a}_{P,V_\zeta}^{(\varepsilon)}(\theta,\phi)$.[25]

(In the ideal case of no noise or an infinite number of time samples, this approximation would become equality.) Hence, the problem is how to estimate θ and ϕ, given $\hat{\mathbf{a}}_{P,V_\zeta}^{(\varepsilon)}$, for each of the nine configurations in Fig. 1 and Table I, with k being any natural number that is prior known.

The unknown scalar c may be eliminated as follows, on account of Eq. (1):

$$\frac{\left[\hat{\mathbf{a}}_{P,V_\zeta}^{(\varepsilon)}\right]_2}{\left[\hat{\mathbf{a}}_{P,V_\zeta}^{(\varepsilon)}\right]_1} = \eta_1^k\, e^{j2\pi(\Delta_\varepsilon/\lambda)\eta_2}, \tag{8}$$

where $[\cdot]_i$ denotes the ith element of the vector inside the square brackets.

For any prior known $\Delta_\varepsilon \in (0, \lambda/2]$,[26] Eq. (8) leads to

TABLE III. Cramér-Rao bounds for the generalized p-u probe's nine configurations. Here, $\tilde{\Delta} := 2\pi(\Delta_\varepsilon/\lambda)$.

Configuration	$2M\frac{P_s}{P_n}\,\text{CRB}_\theta^{(\cdot)}(\theta,\phi)$	$2M\frac{P_s}{P_n}\,\text{CRB}_\phi^{(\cdot)}(\theta,\phi)$
(a) V_x at $(\Delta_x, 0, 0)$	∞	∞
(b) V_x at $(0, \Delta_y, 0)$	$\frac{\left[\cos^{2k}(\phi)\,\sin^{2k}(\theta)+1\right]\left[\tilde{\Delta}^2\,\cos^4(\phi)\,\sin^2(\theta)+k^2\,\sin^2(\phi)\right]}{\tilde{\Delta}^2\,k^2\,\cos^{2k}(\phi)\,\cos^2(\theta)\,\sin^{2k}(\theta)}$	$\frac{\cos^{2-2k}(\phi)\left[\cos^{2k}(\phi)\,\sin^{2k}(\theta)+1\right]\left[\tilde{\Delta}^2\,\sin^2(\theta)\,\sin^2(\phi)+k^2\right]}{\tilde{\Delta}^2\,k^2\,\sin^{2k+2}(\theta)}$
(c) V_x at $(0, 0, \Delta_z)$	$\frac{1+\cos^{2k}(\phi)\,\sin^{2k}(\theta)}{\tilde{\Delta}^2\,\cos^{2k}(\phi)\,\sin^{2k+2}(\theta)}$	$\frac{\cos^{2-2k}(\phi)\left[\cos^{2k}(\phi)\,\sin^{2k}(\theta)+1\right]\left[\tilde{\Delta}^2\,\sin^4(\theta)+k^2\,\cos^2(\theta)\right]}{\tilde{\Delta}^2\,k^2\,\sin^{2k+4}(\theta)\,\sin^2(\phi)}$
(d) V_y at $(\Delta_x, 0, 0)$	$\frac{\left[\sin^{2k}(\phi)\,\sin^{2k}(\theta)+1\right]\left[\tilde{\Delta}^2\,\sin^4(\phi)\,\sin^2(\theta)+k^2\,\cos^2(\phi)\right]}{\tilde{\Delta}^2\,k^2\,\sin^{2k}(\phi)\,\sin^{2k}(\theta)\,\cos^2(\theta)}$	$\frac{\sin^{2-2k}(\phi)\left[\sin^{2k}(\phi)\,\sin^{2k}(\theta)+1\right]\left[\tilde{\Delta}^2\,\sin^2(\theta)\,\cos^2(\phi)+k^2\right]}{\tilde{\Delta}^2\,k^2\,\sin^{2k+2}(\theta)}$
(e) V_y at $(0, \Delta_y, 0)$	∞	∞
(f) V_y at $(0, 0, \Delta_z)$	$\frac{1+\sin^{2k}(\phi)\,\sin^{2k}(\theta)}{\tilde{\Delta}^2\,\sin^{2k}(\phi)\,\sin^{2k+2}(\theta)}$	$\frac{\sin^{2-2k}(\phi)\left[\sin^{2k}(\phi)\,\sin^{2k}(\theta)+1\right]\left[\tilde{\Delta}^2\,\sin^4(\theta)+k^2\,\cos^2(\theta)\right]}{\tilde{\Delta}^2\,k^2\,\sin^{2k+4}(\theta)\,\cos^2(\phi)}$
(g) V_z at $(\Delta_x, 0, 0)$	$\frac{\cos^{2-2k}(\theta)\left[\cos^{2k}(\theta)+1\right]}{k^2\,\cos^2(\theta)}$	$\frac{\left[\cos^{2k}(\theta)+1\right]\left[\tilde{\Delta}^2\,\cos^2(\phi)\,\cos^4(\theta)+k^2\,\sin^2(\theta)\right]}{\tilde{\Delta}^2\,k^2\,\cos^{2k}(\theta)\,\sin^2(\phi)\,\sin^4(\theta)}$
(h) V_z at $(0, \Delta_y, 0)$	$\frac{\cos^{2-2k}(\theta)\left[\cos^{2k}(\theta)+1\right]}{k^2\,\cos^2(\theta)}$	$\frac{\left[\cos^{2k}(\theta)+1\right]\left[\tilde{\Delta}^2\,\sin^2(\phi)\,\cos^4(\theta)+k^2\,\sin^2(\theta)\right]}{\tilde{\Delta}^2\,k^2\,\cos^2(\phi)\,\cos^{2k}(\theta)\,\sin^4(\theta)}$
(i) V_z at $(0, 0, \Delta_z)$	$\frac{\cos^{2-2k}(\theta)\left[\cos^{2k}(\theta)+1\right]}{\sin^2(\theta)\left[\tilde{\Delta}^2\,\cos^2(\theta)+k^2\right]}$	∞

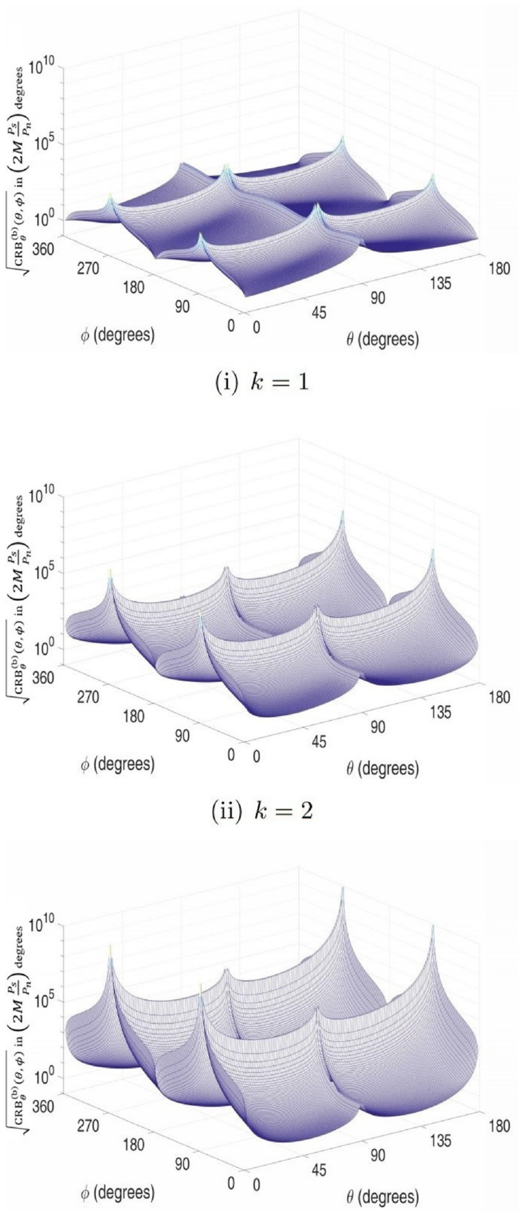

(i) $k=1$

(ii) $k=2$

(iii) $k=3$

FIG. 2. (Color online) Configuration (b): CRB of $\theta\,[\mathrm{CRB}_\theta^{(b)}(\theta,\phi)]$ for various orders (k) of figure-8 sensor. (i) $k=1$, (ii) $k=2$, (iii) $k=3$.

$$\hat{\eta}_1=\left|\frac{\left[\hat{\mathbf{a}}_{P,V_\zeta}^{(\varepsilon)}\right]_2}{\left[\hat{\mathbf{a}}_{P,V_\zeta}^{(\varepsilon)}\right]_1}\right|^{1/k}\operatorname{sgn}(\eta_1),\tag{9}$$

$$\hat{\eta}_2=\frac{\lambda}{2\pi\Delta_\varepsilon}\angle\left(\operatorname{sgn}(\eta_1)\frac{\left[\hat{\mathbf{a}}_{P,V_\zeta}^{(\varepsilon)}\right]_2}{\left[\hat{\mathbf{a}}_{P,V_\zeta}^{(\varepsilon)}\right]_1}\right).\tag{10}$$

If $\Delta_\varepsilon>\lambda/2$, the spatial phase factor $e^{j(2\pi\Delta_\varepsilon/\lambda)\eta_2}$ has no one-to-one mapping with η_2; hence, Eqs. (9) and (10) cannot uniquely estimate both θ and ϕ. However, the extended-aperture methodology can be used to resolve the cases with $\Delta_\varepsilon>\lambda/2$.[27–30]

From the above $\hat{\eta}_1$ and $\hat{\eta}_2$, the closed-form estimates $\hat{\theta}$ and $\hat{\phi}$ are specified in Table II, for $\varepsilon\neq\zeta$.

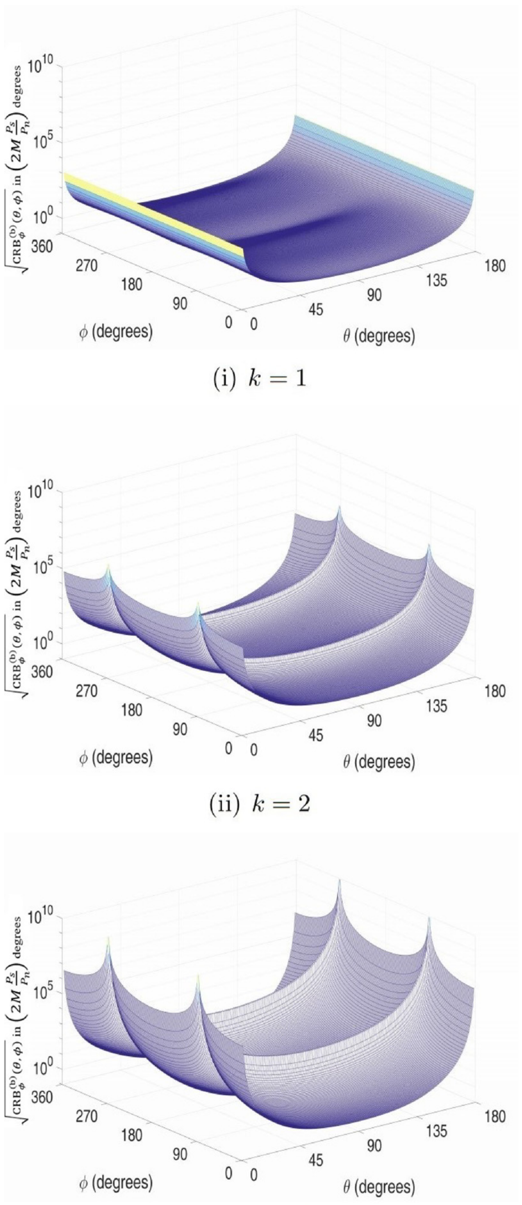

(i) $k=1$

(ii) $k=2$

(iii) $k=3$

FIG. 3. (Color online) Configuration (b): CRB of $\phi\,[\mathrm{CRB}_\phi^{(b)}(\theta,\phi)]$ for various orders (k) of figure-8 sensor. (i) $k=1$, (ii) $k=2$, (iii) $k=3$.

There, due to $\operatorname{sgn}(\eta_1)$ and due to the cyclic ambiguities of inverse trigonometric functions inherent in η_1 and η_2, $\hat{\theta}$ and $\hat{\phi}$ can be unambiguous for only a tetarto-sphere (i.e., a quarter of a sphere). For configuration (b), the necessary prior knowledge is whether $\theta\in[0,\pi/2)$ or $\theta\in[\pi/2,\pi)$ (i.e., upper vs lower hemisphere) and whether $u>0$ or $u<0$ (i.e., front vs back hemisphere). For configuration (c), the necessary prior knowledge is whether $\phi\in[0,\pi)$ or $\phi\in[\pi,2\pi)$ (i.e., right vs left hemisphere) and whether $u>0$ or $u<0$ (i.e., front vs back hemisphere). For configuration (d), the necessary prior knowledge is whether $\theta\in[0,\pi/2)$ or $\theta\in[\pi/2,\pi)$ (i.e., upper vs lower hemisphere) and whether $v>0$ or $v<0$ (i.e., right vs left hemisphere). For configuration (f), the necessary prior knowledge is whether $\phi\in[-\pi/2,\pi/2)$ or $\phi\in[\pi/2,3\pi/2)$ (i.e., front vs back hemisphere) and whether $v>0$ or $v<0$ (i.e., right vs left

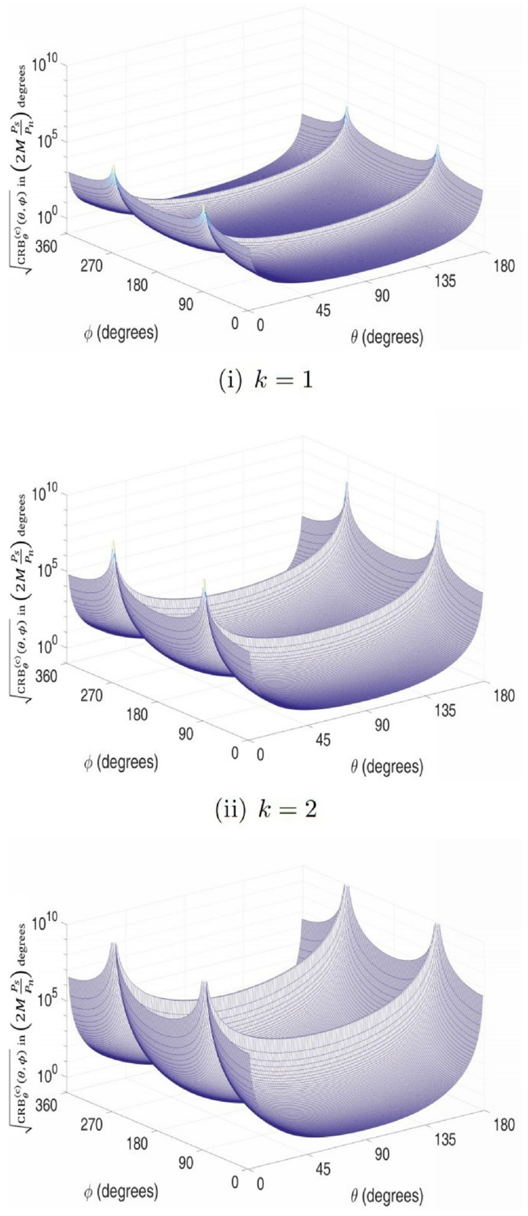

(i) $k=1$

(ii) $k=2$

(iii) $k=3$

FIG. 4. (Color online) Configuration (c): CRB of $\theta\,[\mathrm{CRB}_\theta^{(c)}(\theta,\phi)]$ for various orders (k) of figure-8 sensor. (i) $k=1$, (ii) $k=2$, (iii) $k=3$.

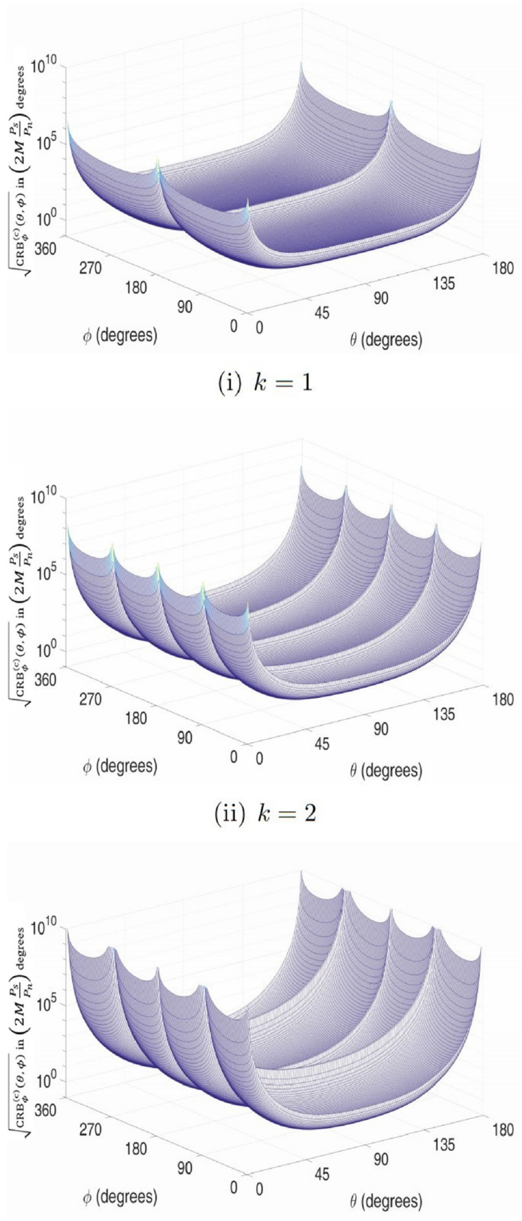

(i) $k=1$

(ii) $k=2$

(iii) $k=3$

FIG. 5. (Color online) Configuration (c): CRB of $\phi\,[\mathrm{CRB}_\phi^{(c)}(\theta,\phi)]$ for various orders (k) of figure-8 sensor. (i) $k=1$, (ii) $k=2$, (iii) $k=3$.

hemisphere). For configuration (g), the necessary prior knowledge is whether $\phi \in [0,\pi)$ or $\phi \in [\pi, 2\pi)$ (i.e., right vs left hemisphere) and whether $w>0$ or $w<0$ (i.e., upper vs lower hemisphere). For configuration (h), the necessary prior knowledge is whether $\phi \in [-\pi/2, \pi/2)$ or $\phi \in [\pi/2, 3\pi/2)$ (i.e., front vs back hemisphere) and whether $w>0$ or $w<0$ (i.e., upper vs lower hemisphere).

At $\theta = 0, \pi$, the impinging signal has none of its energy projected onto the x-y plane; hence, $\hat{\phi}$ would be impossible by any estimator.

If $\eta_1 = \eta_2$, or equivalently if $\varepsilon = \zeta$ [as in configurations (a) and (e) and (i)], the system of equations in Eqs. (9) and (10) would be indeterminable, because the right sides of Eqs. (9) and (10) would be equal, thereby offering only one constraint for two unknowns.

If the two sensors' have their locations switched: The array manifold's multiplicative factor $\left(e^{j2\pi(\Delta_\varepsilon/\lambda)\eta_2}\right)$ will be absorbed into the eigen-composition c, hence poses no change to the estimation formulas there. The array manifold's complex conjugation would result simply in a sign change at the appropriate places of each estimator.

IV. THE CRAMÉR-RAO BOUND FOR THE *K*TH-ORDER P-U PROBE IN VARIOUS CONFIGURATIONS

The Cramér-Rao bound lower-bounds the error variance obtainable from *any* unbiased estimator, given the statistical model that connects the observed data to the unknown parameter being estimated. To focus on the directivity order k and on the spatial configuration, the following analysis will

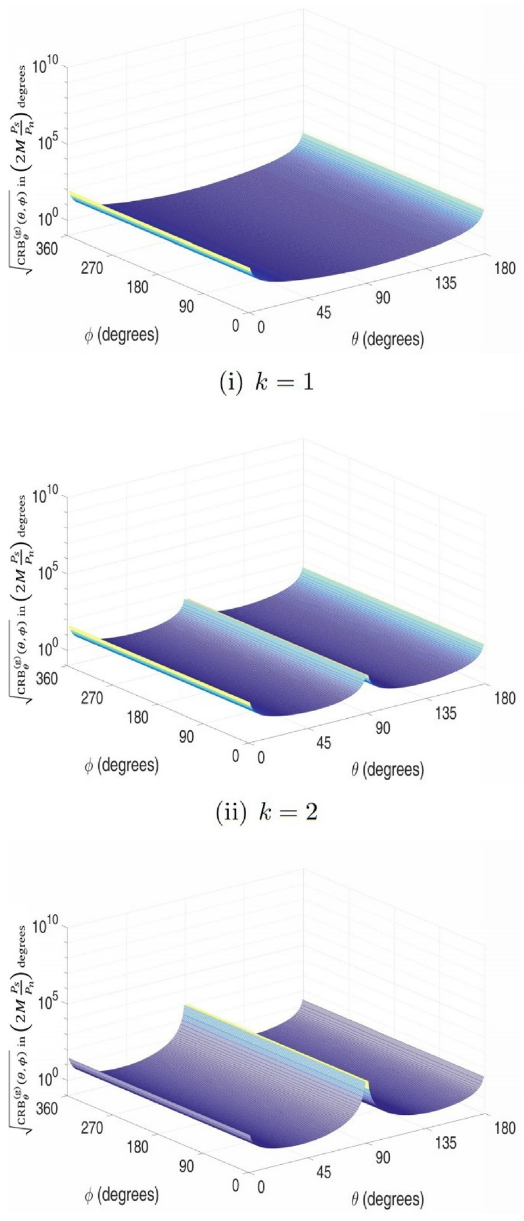

(i) $k=1$

(ii) $k=2$

(iii) $k=3$

FIG. 6. (Color online) Configuration (g): CRB of $\theta\,[\mathrm{CRB}_\theta^{(g)}(\theta,\phi)]$ for various orders (k) of figure-8 sensor. (i) $k=1$, (ii) $k=2$, (iii) $k=3$.

use a simple statistical model for the incident signal and for the corrupting noise. This analysis could be readily extended to more complicated signal/noise scenarios.

Model the incident signal as a pure-tone

$$s(t) = \sqrt{P_s}\, e^{j(\omega t+\varphi)}, \tag{11}$$

where P_s denotes the signal power and φ the initial phase, both deterministic but allowed to be unknown. Let there be additive noise, modeled as Gaussian, zero-mean, statistically uncorrelated over time and across the two component-sensors, with an unknown power of P_n.

At the mth time instant of $t = mT_s$ (where T_s denotes the time-sampling period), the p-u probe provides a 2×1 data vector of

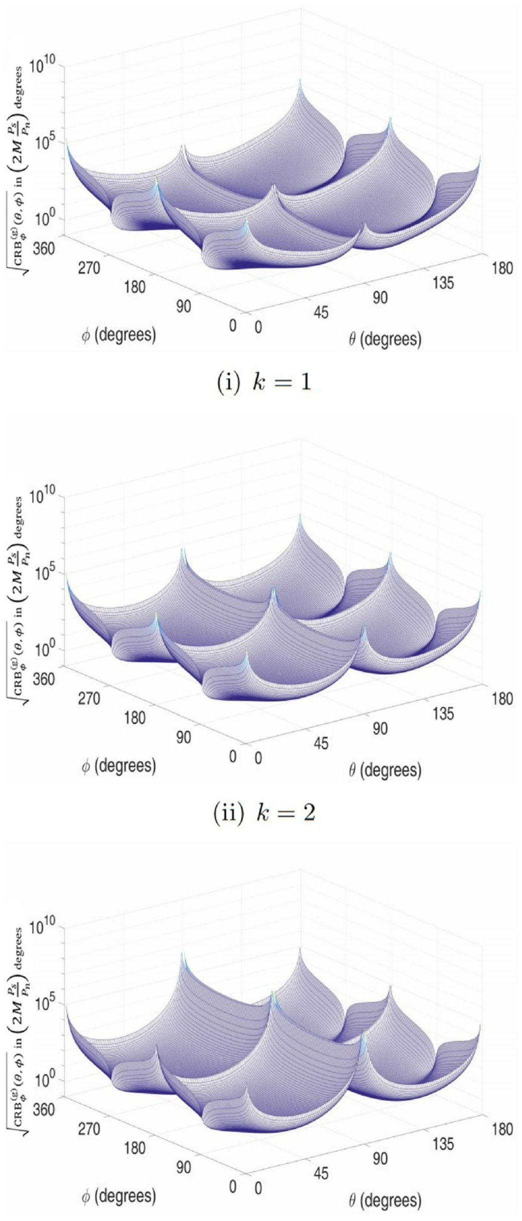

(i) $k=1$

(ii) $k=2$

(iii) $k=3$

FIG. 7. (Color online) Configuration (g): CRB of $\phi\,[\mathrm{CRB}_\phi^{(g)}(\theta,\phi)]$ for various orders (k) of figure-8 sensor. (i) $k=1$, (ii) $k=2$, (iii) $k=3$.

$$\tilde{\mathbf{z}}(mT_s) = \mathbf{a}\, s(mT_s) + \tilde{\mathbf{n}}(mT_s), \quad \forall m = 1, 2, \ldots, M. \tag{12}$$

It is assumed that ω, Δ_ε, and λ are previously known.

This statistical data model has five real-valued scalar unknowns: θ, ϕ, P_s, P_n, φ. Hence, the resulting Fisher

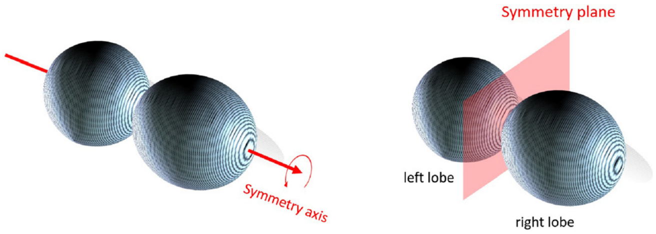

FIG. 8. (Color online) Symmetries in the figure-8 sensor's gain response.

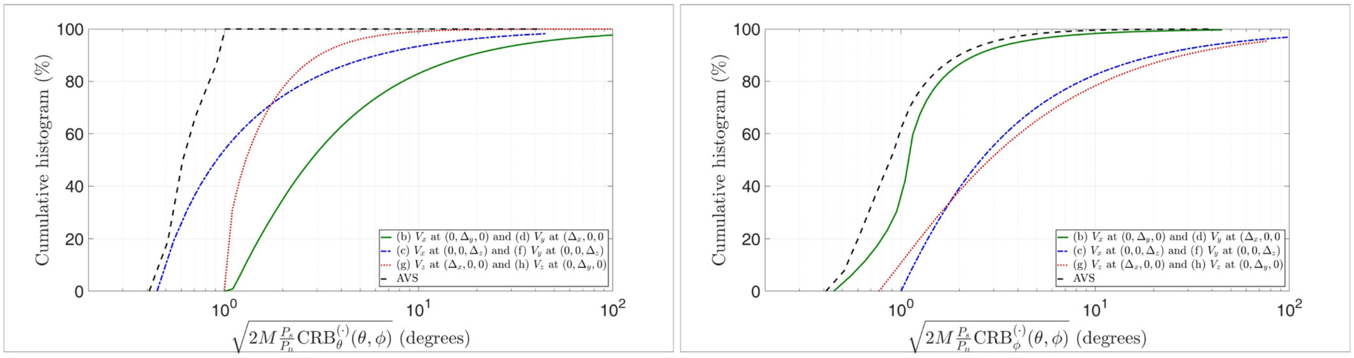

(i) For θ (ii) For ϕ

FIG. 9. (Color online) Cumulative histograms to compare the six configurations with the figure-8 sensor at order $k=1$, vs the customary four-component acoustic vector-sensor (AVS). (i) For θ, (ii) For ϕ.

information matrix (FIM) is 5×5 in size. The corresponding Cramér-Rao bounds are derived (using Sec. 8.2.3.1 of Ref. 31) and stated in Table III. Therein, for example, the superscript in $\mathrm{CRB}_\theta^{(\mathrm{a})}(\theta,\phi)$ refers to configuration (a), whereas the subscript $_\theta$ identifies the to-be-estimated parameter whose Cramér-Rao bound is symbolized.

Figures 2–7 plot the Cramér-Rao bounds at various values of the sensor-order k, for the six configurations that allow bivariate azimuth-elevation direction-of-arrival estimation. The remaining three configurations, shaded in Fig. 1 and Table I, would not allow such bivariate direction finding, for reasons already explained at the end of Sec. III.

A. Inter-relationships among various configurations' Cramér-Rao bounds

Because the various configurations' array manifolds are functionally inter-related as in Eqs. (2)–(5), their corresponding Cramér-Rao bounds are also correspondingly inter-related as follows:

$$(\mathrm{b}) \leftrightarrow (\mathrm{d}): \ \mathrm{CRB}_\times^{(\mathrm{b})}(\theta,\phi) = \mathrm{CRB}_\times^{(\mathrm{d})}\left(\theta, \frac{\pi}{2}-\phi\right), \qquad (13)$$

$$(\mathrm{c}) \leftrightarrow (\mathrm{f}): \ \mathrm{CRB}_\times^{(\mathrm{c})}(\theta,\phi) = \mathrm{CRB}_\times^{(\mathrm{f})}\left(\theta, \frac{\pi}{2}-\phi\right), \qquad (14)$$

$$(\mathrm{g}) \leftrightarrow (\mathrm{h}): \ \mathrm{CRB}_\times^{(\mathrm{g})}(\theta,\phi) = \mathrm{CRB}_\times^{(\mathrm{h})}\left(\theta, \frac{\pi}{2}-\phi\right), \qquad (15)$$

$$(\mathrm{e}) \leftrightarrow (\mathrm{a}): \ \mathrm{CRB}_\times^{(\mathrm{e})}(\theta,\phi) = \mathrm{CRB}_\times^{(\mathrm{a})}\left(\theta, \frac{\pi}{2}-\phi\right), \qquad (16)$$

with the subscript $\times \in \{\theta,\phi\}$.

B. Symmetries in each Cramér-Rao bound

Each Cramér-Rao bound is

(i) symmetric with respect to $\theta = 90^\circ$ over $\theta \in [0^\circ, 180^\circ]$,
(ii) symmetric with respect to $\phi = 0^\circ$ over $\phi \in [-90^\circ, 90^\circ]$,
(iii) symmetric with respect to $\phi = 90^\circ$ over $\phi \in [0^\circ, 180^\circ]$,
(iv) symmetric with respect to $\phi = 180^\circ$ over $\phi \in [90^\circ, 270^\circ]$, and
(v) symmetric with respect to $\phi = 270^\circ$ over $\phi \in [180^\circ, 360^\circ]$.

These symmetries arise mathematically in every Cramér-Rao bound expression due to the even powers to which the trigonometric functions are raised. Physically speaking, these symmetries exist because the figure-8 sensor's gain response (a) has a longitudinal cross-section that is 360° rotationally invariant with regard to the figure-8 sensor's axis, and (b) has two lobes that are left/right symmetric to each other. Please see Fig. 8.

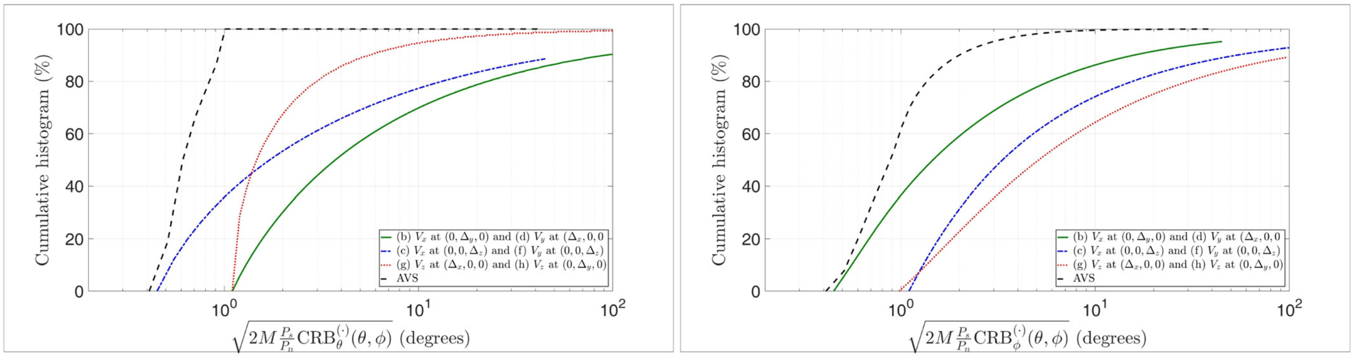

(i) For θ (ii) For ϕ

FIG. 10. (Color online) Cumulative histograms to compare the 6 configurations with the figure-8 sensor at order $k=2$, vs the customary four-component acoustic vector-sensor (AVS). (i) For θ, (ii) For ϕ.

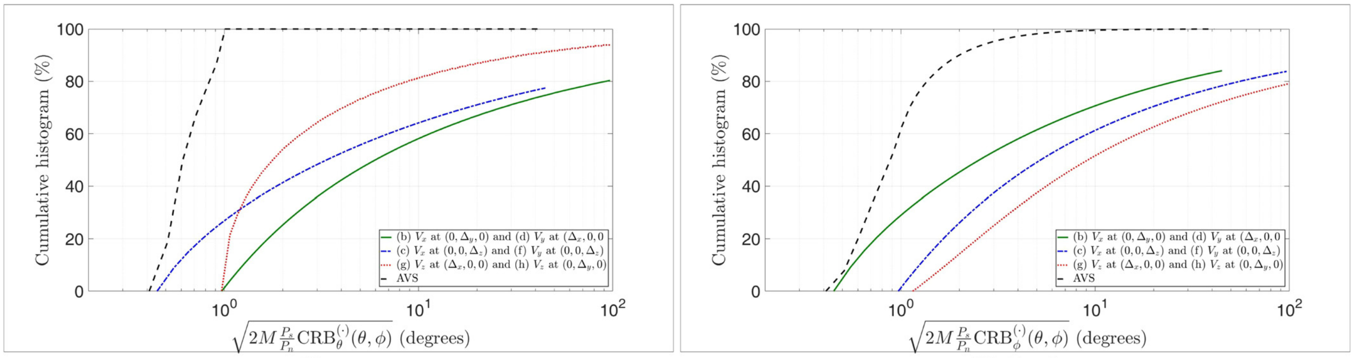

(i) For θ (ii) For ϕ

FIG. 11. (Color online) Cumulative histograms to compare the six configurations with the figure-8 sensor at order $k=3$, vs the customary four-component acoustic vector-sensor (AVS). (i) For θ, (ii) For ϕ.

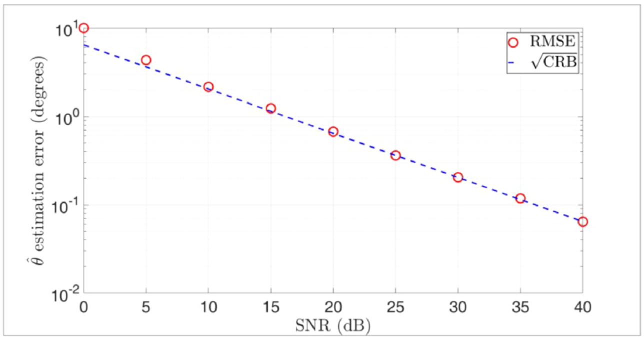

(i) $k = 1$

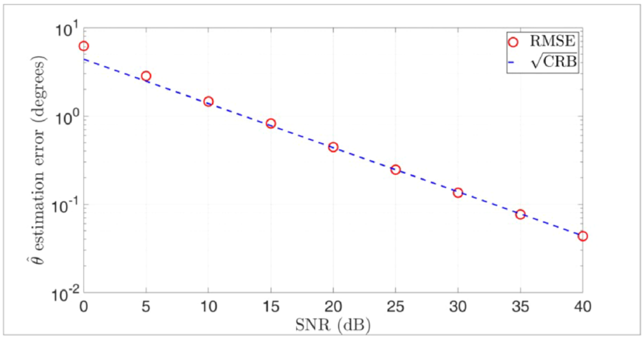

(ii) $k = 2$

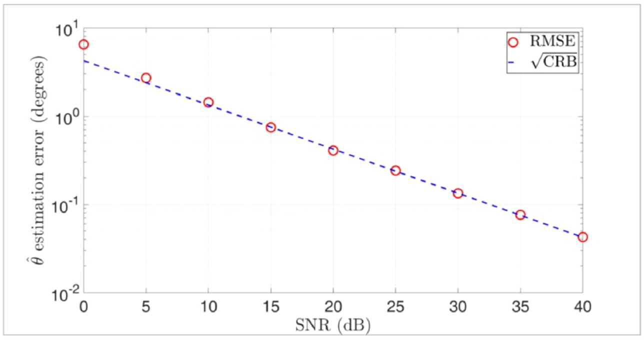

(iii) $k = 3$

FIG. 12. (Color online) Configuration (b): The proposed $\hat{\theta}$'s RMSE vs $\sqrt{\mathrm{CRB}_\theta^{(\mathrm{b})}(\theta,\phi)}$, at various sensor-orders k. (i) $k=1$, (ii) $k=2$, (iii) $k=3$.

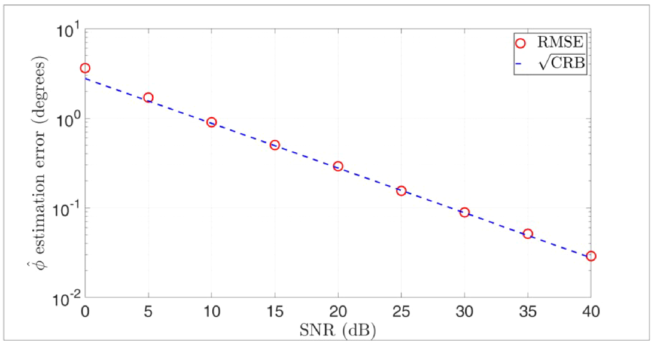

(i) $k = 1$

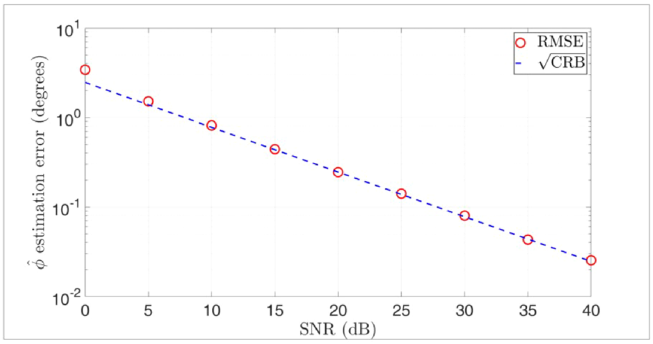

(ii) $k = 2$

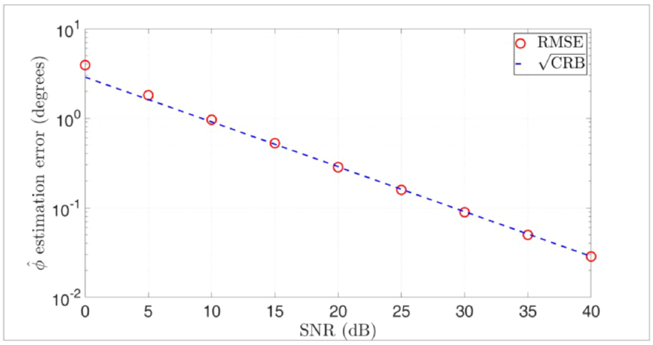

(iii) $k = 3$

FIG. 13. (Color online) Configuration (b): The proposed $\hat{\phi}$'s RMSE vs $\sqrt{\mathrm{CRB}_\phi^{(\mathrm{b})}(\theta,\phi)}$, at various sensor-orders k. (i) $k=1$, (ii) $k=2$, (iii) $k=3$.

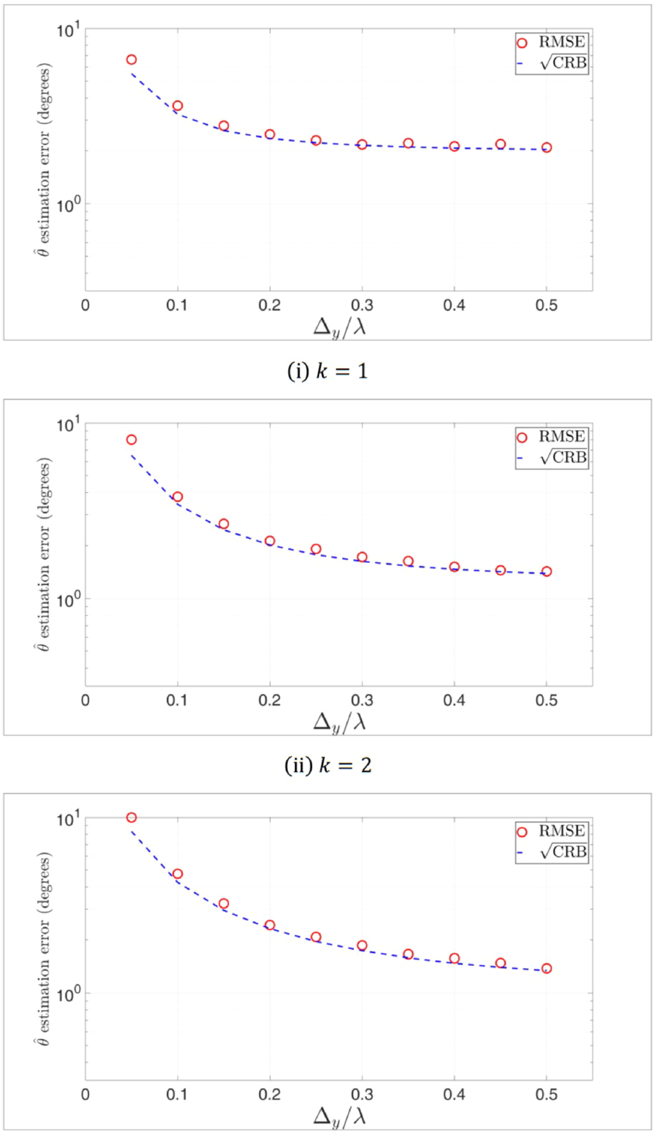

(i) $k = 1$

(ii) $k = 2$

(iii) $k = 3$

FIG. 14. (Color online) Configuration (b): The proposed $\hat{\theta}$'s RMSE and $\sqrt{\text{CRB}_\theta^{(b)}(\theta,\phi)}$ vs sensor's separation Δ_y/λ, at various sensor-orders k. (i) $k=1$, (ii) $k=2$, (iii) $k=3$.

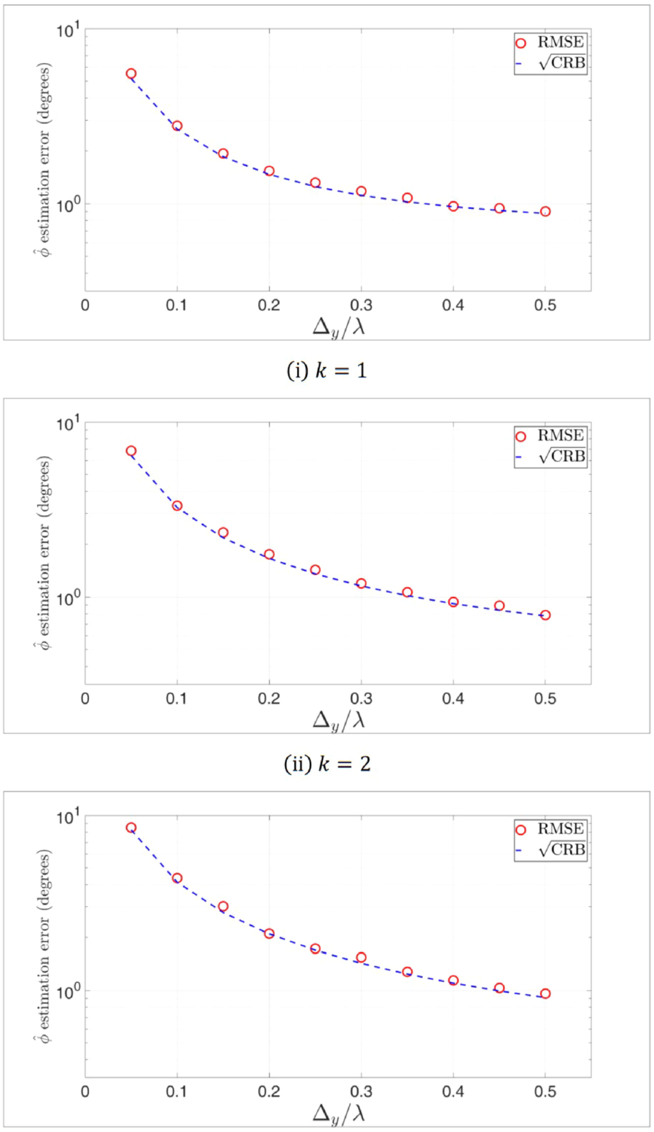

(i) $k = 1$

(ii) $k = 2$

(iii) $k = 3$

FIG. 15. (Color online) Configuration (b): The proposed $\hat{\phi}$'s RMSE and $\sqrt{\text{CRB}_\phi^{(b)}(\theta,\phi)}$ vs sensor's separation Δ_y/λ, at various sensor-orders k. (i) $k=1$, (ii) $k=2$, (iii) $k=3$.

C. To compare across the various configurations in Fig. 1 and Table I

To compare across various configurations by their direction-finding precision: Figs. 9–11 plot the Cramér-Rao bound's cumulative histogram, which reveals the percentage of all possible incident direction-of-arrival from the two-dimensional support region of $\{\theta \in [0,\pi]\} \cup \{\phi \in [0,2\pi)\}$, at which the corresponding configuration can estimate better than or equal to the precision specified by the abscissa. Figure 9 is for sensor-order $k=1$, Fig. 10 for $k=2$, and Fig. 11 for $k=3$. Each figure compares all six configurations (i.e., all those that allow bivariate direction finding); nonetheless, the identities in Eqs. (13)–(15) imply only three *distinct* cumulative histogram curves for each of Figs. 9–11. These cumulative histograms are computed here using spatially uniform sampling over the unit-sphere's surface $\forall(\theta,\phi)$, i.e., a equal number of uniformly spaced samples per any unit area on the unit-sphere's surface.[32] The number of spatial samples equals 1.5×10^6 over the spherical surface. Recall that the Cramér-Rao bound represents the hypothetically best precision obtainable in estimating the direction-of-arrival: the smaller the Cramér-Rao bound the better, hence the higher the cumulative histogram the better.

Some qualitative observations on $\text{CRB}_\theta^{(\cdot)}(\theta,\phi)$:

(1) Configuration (b)'s $\text{CRB}_\theta^{(b)}(\theta,\phi)$ and configuration (d)'s $\text{CRB}_\theta^{(d)}(\theta,\phi)$ are worse than the other configurations' $\text{CRB}_\theta^{(\cdot)}(\theta,\phi)$. This is intuitively reasonable, because these two configurations:
  (i) *orient* the figure-8 directional sensor to yield *no* θ-directivity, and
  (ii) *space* the two component-sensors to yield *no* vertical aperture.

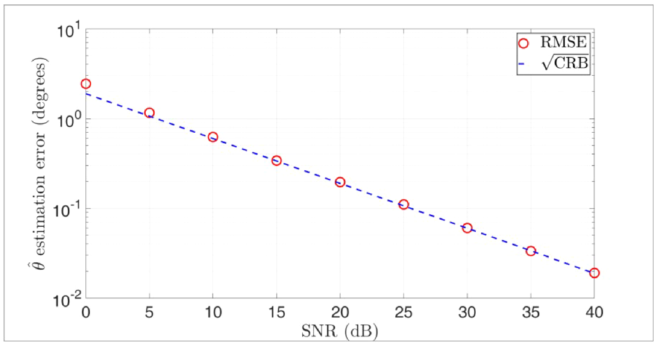

(i) $k = 1$

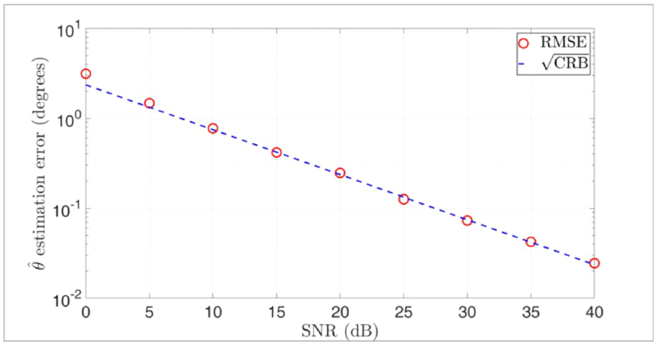

(ii) $k = 2$

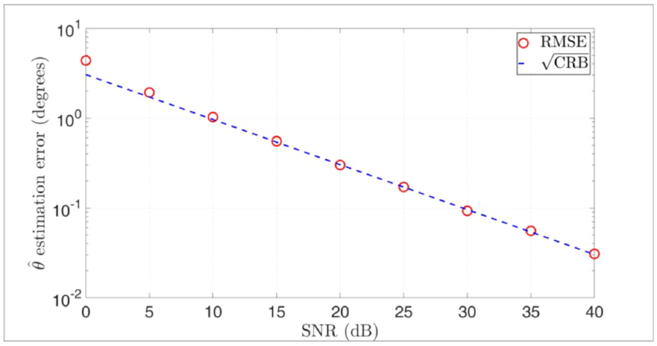

(iii) $k = 3$

FIG. 16. (Color online) Configuration (c): The proposed $\hat{\theta}$'s RMSE vs $\sqrt{\text{CRB}_{\theta}^{(c)}(\theta,\phi)}$, at various sensor-orders k. (i) $k=1$, (ii) $k=2$, (iii) $k=3$.

(2) Configurations (g)'s and (h)'s cumulative histogram is crossed over by that of configurations (c) and (f), as the abscissa gets sufficiently large. Moreover, this cross-over abscissa drops, as the directivity order k increases. The explanation is as follows: Configurations (c) and (f) provide an inter-sensor spatial aperture along the vertical, but no vertical directivity exists in its figure-8 sensor. In contrast, configurations (g) and (h) offer vertical directivity but no vertical aperture. Figures 9–11 indicate that a $\lambda/2$ vertical aperture is more important than the vertical directivity, to attain a very low Cramér-Rao bound for selected (θ,ϕ) sectors. However, this advantage diminishes, as the directivity order k increases, when configurations (c) and (f) become decisively better than configurations (g) and (h). Configurations (c) and (f) provide a horizontal directivity, but *no* horizontal aperture. In contrast, configurations (g) and (h) offer *no* horizontal directivity but a horizontal aperture. As discussed above, the figure-8 sensor directivity is more important to attain the lowest Cramér-Rao bound for selected (θ,ϕ) sectors. A sufficiently high k could dominate any lack of aperture.

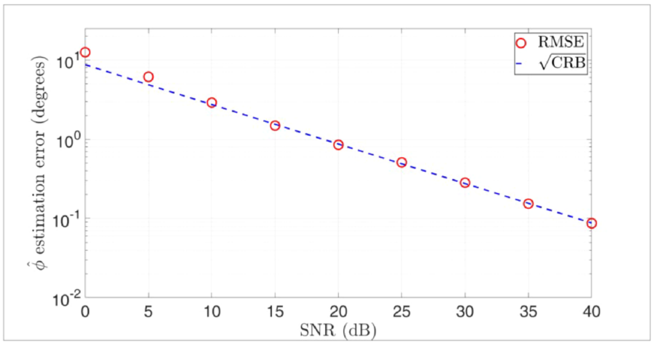

(i) $k = 1$

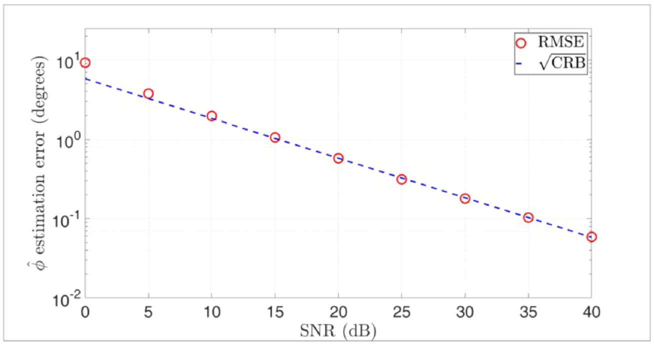

(ii) $k = 2$

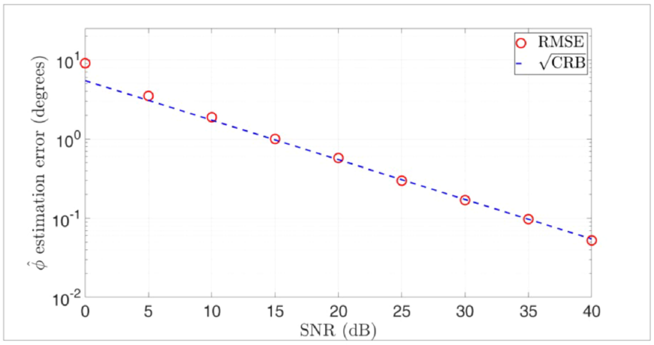

(iii) $k = 3$

FIG. 17. (Color online) Configuration (c): The proposed $\hat{\phi}$'s RMSE vs $\sqrt{\text{CRB}_{\phi}^{(c)}(\theta,\phi)}$, at various sensor-orders k. (i) $k=1$, (ii) $k=2$, (iii) $k=3$.

Some qualitative observations on $\text{CRB}_{\phi}^{(\cdot)}(\theta,\phi)$:

(3) For $\text{CRB}_{\phi}^{(\cdot)}(\theta,\phi)$, configurations (b) and (d) are better than the other configurations. This is also intuitively reasonable, because these two configurations
   (i) *orient* the figure-8 directional sensor to maximize ϕ-directivity, as well as
   (ii) *space* the two component-sensors to give maximum *horizontal* inter-sensor aperture.

(4) Configurations (g) and (h)'s cumulative histogram crosses over that of configurations (c) and (f), as the abscissa gets sufficiently large. Moreover, this cross-over abscissa drops, as the directivity order k increases. The explanation is exactly same as that under point (2) above.

(5) The Cramér-Rao bounds would be unaffected by any switch of the two component-sensors' locations.

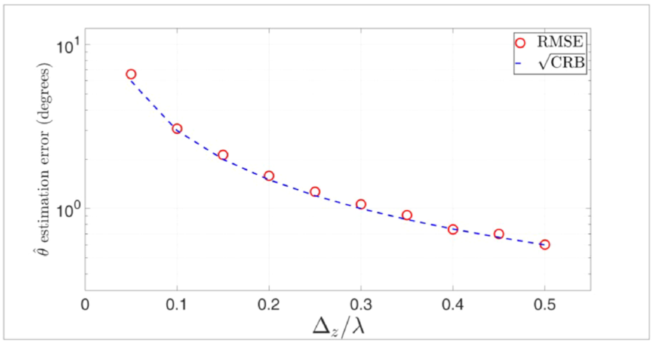

(i) $k = 1$

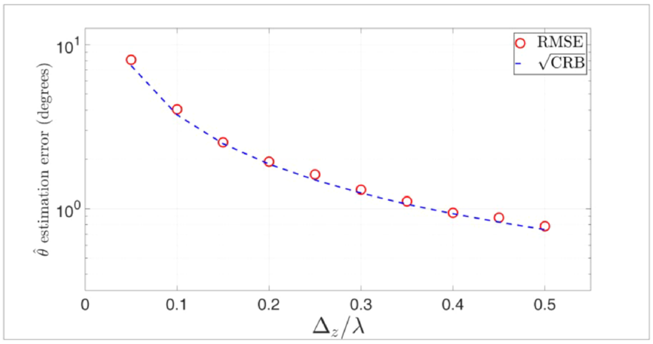

(ii) $k = 2$

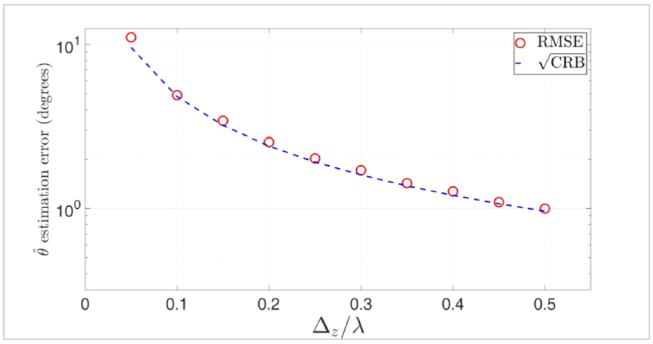

(iii) $k = 3$

FIG. 18. (Color online) Configuration (c): The proposed $\hat{\theta}$'s RMSE and $\sqrt{\text{CRB}_\theta^{(c)}(\theta,\phi)}$ vs sensor's separation Δ_z/λ, at various sensor-orders k. (i) $k = 1$, (ii) $k = 2$, (iii) $k = 3$.

Last:

(6) The four-component acoustic vector-sensor (AVS), comprising a tri-axial velocity-sensor and a collocating pressure-sensor, offers better Cramér-Rao bounds, than any of the high-order p-u probes. This is unsurprising, because the acoustic vector-sensor has more component-sensors.

V. MONTE CARLO SIMULATIONS OF THE ESTIMATORS PROPOSED IN SEC. III

This section presents Monte Carlo simulations of the estimator proposed in Sec. III for configuration (b), as an illustrative example. These simulations show the estimator's efficacy, with an estimation error variance very close to the Cramér-Rao bound derived in Sec. IV.

The statistical data model of Sec. IV is retained here. Moreover, $\Delta_\varepsilon/\lambda = 1/2$, $\omega = 1885$ radians/s, and $\varphi = 0$.

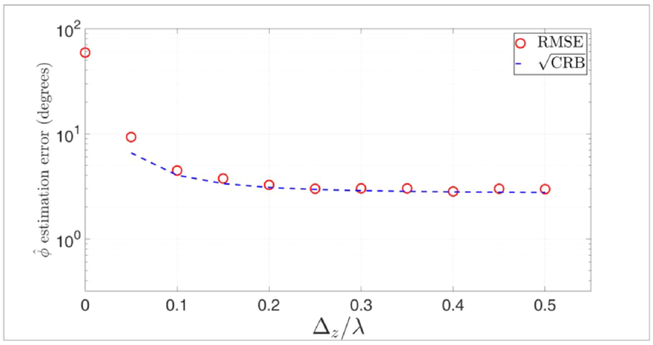

(i) $k = 1$

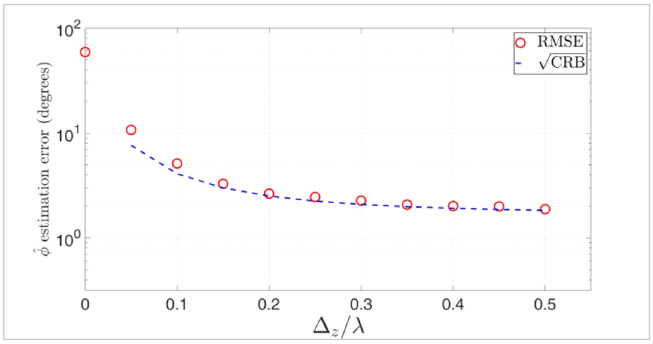

(ii) $k = 2$

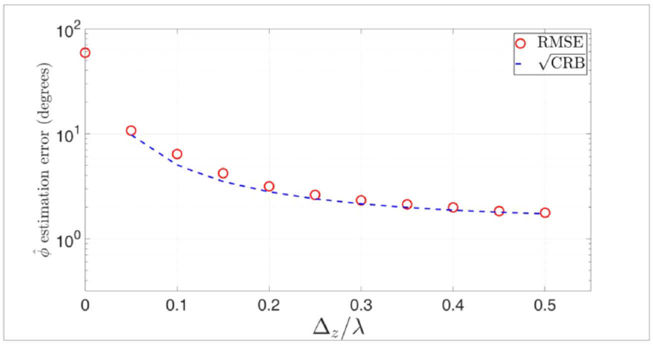

(iii) $k = 3$

FIG. 19. (Color online) Configuration (c): The proposed $\hat{\phi}$'s RMSE and $\sqrt{\text{CRB}_\phi^{(c)}(\theta,\phi)}$ vs sensor's separation Δ_z/λ, at various sensor-orders k. (i) $k = 1$, (ii) $k = 2$, (iv) $k = 3$.

Figures 12–15 compare configuration (b)'s estimators in the second row of Table II, against the corresponding Cramér-Rao bounds in the second row of Table III. Each icon on each figure represent 1000 independent Monte Carlo trials. These figures unanimously verify the proposed estimator's efficacy and closeness to the Cramér-Rao bounds. Figures 16–19 do the same for configuration (c)'s estimators in the third row of Table II, against the corresponding Cramér-Rao bounds in the third row of Table III.

Figures 12 and 13 and 16 and 17 show that the Cramér-Rao bounds decrease (i.e., improve) as the SNR increases for $k = 1$, 2, 3, as would be expected. Figures 14 and 15 and 18 and 19 show that the Cramér-Rao bounds also decrease as the inter-sensor spacing Δ_ε increases (and thus the array aperture is enlarged) for $k = 1$, 2, 3, as also would be expected.

VI. CONCLUSION

This paper generalizes the customary p-u probe, in various configurations, as an acoustical sensing system for azimuth-elevation direction finding. New eigen-based direction-finding signal-processing algorithms are advanced here in closed form. These algorithms, developed here for a single generalized p-u pair, could be used for a multiple-pair array, thereby relaxing the support-region restrictions. Deterministic Cramér-Rao bound analysis compares these various configurations, at various orders of sensor directivity, by their relative precision for direction finding, at various orders of sensor directivity. Comparing between the customary p-u probe and the high-order generalization here: the latter's array manifold has a power of k, which fundamentally changes the obtainable Cramér-Rao bound, in ways that are analyzed in Sec. IV C's observations (1) to (6): If azimuthal resolution is *somewhat* (but not categorically) more (less) important than the elevational resolution, use a high-order figure-8 sensor in a horizontal (vertical) orientation but in vertical (horizontal) displacement from the omnidirectional pressure-sensor. If the azimuthal resolution is *categorically* more important than the elevational resolution, use Configurations (b) and (d). Besides the figure-8 sensor, other directional sensors could be investigated by the interested reader, e.g., the "cardioids"[35] or the "hypoids."[36]

ACKNOWLEDGMENT

The authors would like to thank Dr. William C. Kirkpatrick Alberts and Dr. Yang Song for useful discussions. The authors would like to thank Chibuzo Joseph Nnonyelu for helping with the Latex word-processing.

[1] Y. Song, Y. L. Li, and K. T. Wong, "Acoustic direction finding using a pressure sensor and a uniaxial particle velocity sensor," IEEE Trans. Aerosp. Electron. Syst. **51**, 2560–2569 (2015).

[2] H. F. Olson, *Acoustical Engineering* (Van Nostrand, Princeton, NJ, 1957), Chap. 8, pp. 246–339.

[3] Y. Huang and J. Benesty, *Audio Signal Processing for Next Generation Multimedia Communication Systems, Part I: Speech Acquisition and Enhancement* (Kluwer Academic, New York, 2004), Chap. 2, pp. 11–65.

[4] Y. Song and K. T. Wong, "Closed-form direction finding using collocated but orthogonally oriented higher order acoustic sensors," IEEE Sensors J. **12**, 2604–2608 (2012).

[5] A. J. Brouns, "Second-order gradient noise-cancelling microphone," in *IEEE International Conference on Acoustics, Speech, and Signal Processing*, Georgia (1981), pp. 786–789.

[6] H. E. de Bree, "An overview of microflown technologies," Acta Acust. Acust. **89**, 163–172 (2003).

[7] H. F. Olson, "Electroacoustical signal translating apparatus," U.S. patent 2,301,744 (May 31, 1941).

[8] A. M. Wiggins, "Second order differential microphone," U.S. patent 2,529,467 (November 07, 1950).

[9] A. M. Wiggins, "Second order differential microphone," U.S. patent 2,552,878 (May 15, 1951).

[10] A. M. Wiggins, "Higher order pressure gradient microphone system having adjustable polar response pattern," U.S. patent 2,896,189 (July 21, 1959).

[11] M. M. Rosenfeld, "Pressure gradient transducers," U.S. patent 3,068,328 (December 11, 1962).

[12] D. M. Warren and S. C. Thompson, "Microphone array having a second order directional pattern," U.S. patent application 2003/014283 (July 31, 2003).

[13] S. A. Klinke, "Directional microphone arrangement and method for signal processing in a directional microphone arrangement," U.S. patent application 2003/0174852 (September 18, 2003).

[14] R. Miles, "High-order directional microphone diaphragm," U.S. patent 6,963,653 (November 8, 2005).

[15] S. A. Klinke, "Directional-microphone and method for signal processing in same," U.S. patent 7,120,262 (October 10, 2006).

[16] D. M. Warren, "Microphone array having a second order directional pattern," U.S. patent 7,471,798 (December 30, 2008).

[17] B. R. Beavers and R. Brown, "Third order gradient microphone for speech reception," in *38th Convention of the Audio Engineering Society*, Los Angeles (1970), pp. 636–640.

[18] P. C. Hines, A. L. Rosenfeld, B. H. Maranda, and D. L. Hutt, "Evaluation of the endfire response of a superdirective line array in simulated ambient noise environments," in *OCEANS 2000 MTS/IEEE Conference and Exhibition* (2000), Rhode Island, pp. 1489–1494.

[19] Y. Song, K. T. Wong, and Y. L. Li, "Direction finding using a biaxial particle-velocity sensor," J. Sound Vib. **340**, 354–367 (2015).

[20] Y. I. Wu, K. T. Wong, S.-K. Lau, X. Yuan, and S. K. Tang, "A directionally tunable but frequency-invariant beamformer on an acoustic velocity-sensor triad to enhance speech perception," J. Acoust. Soc. Am. **131**, 3891–3902 (2012).

[21] T.-C. Lin, K. T. Wong, M. O. Cordel, and J. P. Ilao, "Beamforming pointing error of a triaxial velocity sensor under gain uncertainties," J. Acoust. Soc. Am. **140**, 1675–1685 (2016).

[22] A. Nehorai and E. Paldi, "Acoustic vector-sensor array processing," IEEE Trans. Signal Process. **42**, 2481–2491 (1994).

[23] Y. I. Wu, K. T. Wong, and S.-K. Lau, "The acoustic vector-sensor's near-field array-manifold," IEEE Trans. Signal Process. **58**, 3946–3951 (2010).

[24] Y. I. Wu, S.-K. Lau, and K. T. Wong, "Near-field/far-field array manifold of an acoustic vector-sensor near a reflecting boundary," J. Acoust. Soc. Am. **139**, 3159–3176 (2016).

[25] Suppose a signal $s(t)$ reaches the p-u probe, but becomes corrupted additively by the p-u probe's thermal noise-vector $\mathbf{n}(t)$. The p-u probe's measurement then equals to a 2×1 data vector of $\mathbf{z}(t_m) = s(t_m)\mathbf{a} + \mathbf{n}(t_m)$ at the mth time sample. From M such time samples, a data correlation matrix of $\hat{\mathbf{C}} = \sum_{m=1}^{M} \mathbf{z}(t_m)[z(t_m)]^H$ is formed, where the superscript ^{H} symbolizes the Hermitian operator. Suppose further that $\{s(t)\}$ and $\{\mathbf{n}(t)\}$ are each temporally stationary and not cross-correlated between them. Then, $\hat{\mathbf{C}} \approx \mathbf{C} = MP_s\mathbf{a}\mathbf{a}^H + MP_n\mathbf{I}$, where P_s denotes the power of the incident signal, $\mathbf{a}$ symbolizes the impinging source's steering vector, P_n refers to the thermal noise power at each component-sensor, and $\mathbf{I}$ signifies a 2×2 identity matrix. This 2×2 matrix $\hat{\mathbf{C}}$ is Hermitian, and asymptotically approaches $\mathbf{C}$ as $M \to \infty$. The asymptotic $\hat{\mathbf{C}}$ has a principal eigenvector equal to $c\mathbf{a}$, where c is some complex-valued scalar that is algebraically independent of $\mathbf{a}$.

[26] If $\Delta_\varepsilon = 0$ (i.e., if the two sensors are collocated at one point in space), η_2 cannot be estimated in Eq. (10), even though η_1 may still be estimated via Eq. (9).

[27] K. T. Wong and M. D. Zoltowski, "Closed-form underwater acoustic direction-finding with arbitrarily spaced vector-hydrophones at unknown locations," IEEE J. Ocean. Eng. **22**, 566–575 (1997).

[28] K. T. Wong and M. D. Zoltowski, "Extended-aperture underwater acoustic multisource azimuth/elevation direction-finding using uniformly but sparsely spaced vector hydrophones," IEEE J. Ocean. Eng. **22**, 659–672 (1997).

[29] K. T. Wong and M. D. Zoltowski, "Self-initiating MUSIC-based direction finding in underwater acoustic particle velocity-field beamspace," IEEE J. Ocean. Eng. **25**, 262–273 (2000).

[30] M. D. Zoltowski and K. T. Wong, "Closed-form eigenstructure-based direction finding using arbitrary but identical subarrays on a sparse uniform rectangular array grid," IEEE Trans. Signal Process. **48**, 2205–2210 (2000).

[31] H. L. Van Trees, *Detection, Estimation, and Modulation Theory, Part IV: Optimum Array Processing* (Wiley-Interscience, New York, 2002), pp. 1–1406.

[32] I. I. Gringorten and P. J. Yepez, "The division of a circle or spherical surface into equal-area cells or pixels," Report No. PL-TR-92-2167 IP, No. 343, Phillips Lab Hanscom Air Force Base, Bedford, MA, 1992.

[33] P. K. Tam and K. T. Wong, "Cramér-Rao Bounds for direction finding by an acoustic vector sensor under nonideal gain-phase responses, noncollocation, or nonorthogonal orientation," IEEE Sensors J. **9**, 969–982 (2009).

[34] Y. Song and K. T. Wong, "Azimuth-elevation direction finding using a microphone and three orthogonal velocity sensors as a non-collocated subarray," J. Acoust. Soc. Am. **133**, 1987–1995 (2013).

[35] K. T. Wong, C. J. Nnonyelu, and Y. I. Wu, "A triad of cardioid sensors in orthogonal orientation and spatial collocation—Its spatial-matched-filter-type beam-pattern," accepted to appear in IEEE Trans. Signal Process. **66**(4), 895–906 (2017).

[36] K. B. Smith and A. V. van Leijen, "Steering vector sensor array elements with linear cardioids and nonlinear hippioids," J. Acoust. Soc. Am. **122**, 370–377 (2007).